scientific reports

Check for updates

OPEN

The anatomy of magnetic field pulse induced transverse domain wall dynamics

Jaehun Cho[1,2], Won Seok Yun[1,2] & June-Seo Kim[1]✉

The microscopic anatomy of the precessional torque-induced magnetic domain wall racetrack memory is numerically investigated. A systematic analysis is performed to explain the efficiency and limitations of this domain wall motion architecture. A transverse domain wall in an in-plane magnetic nanowire is chosen, and the direction of the applied magnetic field is applied to be perpendicular to the film plane. The domain wall displacement upon the application of an out-of-plane magnetic field pulses is shown to be driven by the precessional torque and subsequently decelerated by the damping torque, causing the domain wall to settle at a specific position. Crucially, a characteristic frequency is exhibited by this domain wall dynamics. After removing the magnetic field, a reverse domain wall dynamics is observed with the same frequency, causing the domain wall to revert to its original position. To realize continuous domain wall motion, a notch structure is introduced, and the depinning field is calculated as a function of the out-of-plane field strength. The analysis reveals that the depinning field decreases linearly as the out-of-plane field strength increases. Finally, the principle of domain wall hopping in a multiple-notched nanowire is verified by the application of sequential out-of-plane field pulses.

Magnetic domain walls (DWs) are consistently highlighted as a promising candidate for next-generation non-volatile memory devices due to the capabilities to manipulate them electrically for information storage such as memory devices. Especially, the current-induced motion of DWs is leveraged, where the DWs themselves act as the mobile data storage units for binary information. This technique enables faster and more energy-efficient reading and writing compared to conventional methods, while the magnetic domains ensure data retention without constant power[1–4].

Beyond the memory application field, substantial research efforts are actively being directed toward utilizing the current-induced magnetic DW motion and the magnetic domains (which serve as binary information carriers, typically represented as "UP" or "DOWN" magnetization states) to realize low-power logic circuit components. This research aims to integrate the non-volatility and high density associated with DW-based technology into computing architectures, potentially leading to advanced spintronic memory-in-logic applications[5–10].

While current-induced manipulation of DWs in magnetic nanowires is highly attractive, it is fundamentally inefficient. Magnetic materials inherently possess high resistivity compared to common metals, leading to significant device resistance. The resulting Joule heating is a major issue, as it generates substantial additional power consumption and degrades the reliability and lifetime of the magnetic domains used for information storage[11–13].

To prevent the issues associated with Joule heating, field-driven DW motion is proposed. In this approach, an externally applied magnetic field acts on all spins within the magnetic nanowire, not just the DW itself, making the process highly efficient without generating additional power consumption. However, its industrial implementation is challenging. For the fabrication of complex, high-density devices required by industry (consisting of massive arrays of nanowires), the technology to apply a uniform magnetic field selectively to specific nanowires to control DW motion is technologically restrictive and difficult to develop.

To address all these issues, the technique of precessional torque induced DW motion is introduced. The core principle involves manipulating the DWs using a precessional torque generated by applying a magnetic field pulse perpendicular to the magnetization direction. This requisite magnetic field is generated by injecting a current into highly conductive, low-resistivity nanowires placed adjacent to the magnetic nanowire[14–17]. This method, by exclusively utilizing precessional torque, is highly efficient and is particularly advantageous for fabricating devices based on magnetic materials with a very small magnetic damping constant (such as permalloy, Py). Furthermore, this rotational torque is direction-dependent, varying with the chirality of asymmetric domain walls (e.g., a transverse DW). This dependence introduces a new degree of freedom, enabling the realization

[1]Division of Nanotechnology, Daegu Gyeongbuk Institute of Science and Technology (DGIST), Daegu 42988, Republic of Korea. [2]Jaehun Cho and Won Seok Yun are contributed equally. ✉email: spin2mtj@dgist.ac.kr

of novel device architectures that utilize both the position and the chirality state of the DWs for information processing.

In this study, the microscopic anatomy of the precessional torque induced magnetic domain wall (DW) racetrack is numerically investigated. A systematic analysis is performed to elucidate the efficiency and limitations of this new paradigm for DW motion architecture. To concentrate the investigation on a specific DW motion system within a nanowire, an in-plane magnetic transverse DW is selected, and the direction of the magnetic field application is restricted to be perpendicular to the film plane (Out-of-Plane, OOP).

The results show that the displacement of the DW upon the application of an OOP field is driven by the precessional torque and subsequently decelerated by the damping torque, causing the DW to settle at a specific position. Crucially, this DW dynamics exhibits a characteristic frequency. When the magnetic field is turned off, a DW dynamics with the same frequency acts in the reverse direction, causing the DW to revert to its original position. To realize continuous DW motion, a notch structure is introduced, and the depinning field is calculated as a function of the OOP field strength. The analysis reveals that the depinning field decreases linearly as the OOP field strength increases. Finally, the study verifies the principle of DW hopping in a multiple-notched nanowire by applying sequential OOP field pulses.

Simulation details

The modeling for out-of-plane magnetic field

In this study, two individual simulation tools are employed. Figure 1 presents the simulation geometry and the calculated magnetic field distributions generated by the applied current. As shown in Fig. 1a, a magnetic nanowire containing a transverse magnetic domain wall is positioned between two Au strip lines. Currents flowing in opposite directions are applied to the two Au nanowires to generate a uniform out-of-plane (OOP) Oersted field. The OOP magnetic field calculations are performed using the electric/magnetic field module of "COMSOL Multiphysics," a finite-element-method (FEM) based simulation tool[18].

Figure 1b shows the *YZ*-plane cross-section of the magnetic field distribution calculated using the FEM simulation tool. Currents are applied in opposite directions through the two Au strip lines, with a Py nanowire (100 nm width, 10 nm thickness) located between them. The distance between the two electrodes and the Py nanowire is fixed at 50 nm. The magnetic field strength and distribution along the *x*-direction corresponding to the current applied to the Au electrodes are depicted in Fig. 1c. The gray area represents the Py nanowire where the OOP magnetic field is applied. Although the magnetic field generated by each electrode decreases as 1/distance, the superposition of the Oersted fields generated from the oppositely-biased electrodes results in the uniform OOP field profile shown. The magnetic field measured at the center of the Py nanowire increases proportionally to the current density, reaching a strength of approximately $B_{\mathrm{OOP}} \approx 100$ mT with $J = 1.5 \times 10^{12}$ A/m^2. To achieve a high magnetic field magnitude while avoiding steep magnetic field gradients that could lead to non-uniform dynamics, the distance between the Au strip lines and the magnetic nanowire is optimized at 50 nm.

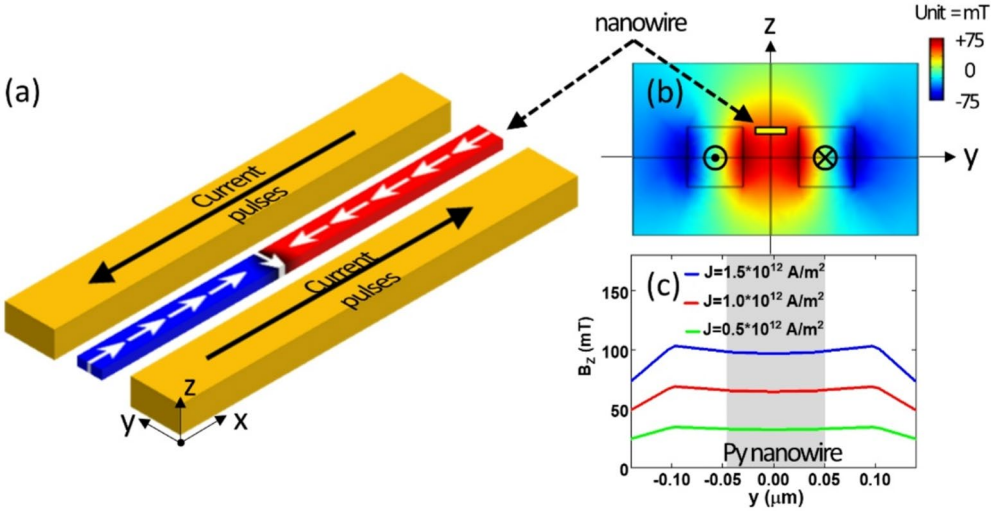

Fig. 1. Simulation geometry and out-of-plane magnetic field distribution. (**a**) Schematic illustration of the simulation geometry including a transverse domain wall (TW) positioned between two Au strip lines. Currents flowing in opposite directions are applied to the Au electrodes to generate a uniform out-of-plane (OOP) Oersted field. (**b**) Two-dimensional contour plot of the magnetic field strength calculated using COMSOL Multiphysics. (**c**) Calculated out-of-plane magnetic field (B_z) line profiles along the *y*-direction for various current densities (J=0.5, 1.0, and 1.5 A/m^2). The gray shaded region represents the position of the Py nanowire with a width of 100 nm.

The details for micromagnetic simulations

To model the transverse wall (TW) dynamics, the "Object-Oriented Micromagnetic Framework (OOMMF)," a finite-difference-method (FDM) based simulation tool, is used[19]. A Py nanowire with a length of 10 μm and a fixed thickness of 10 nm is introduced. The standard material parameter values for Py are used in the simulations: the saturation magnetization $M_s = 8.0 \times 10^5$ A/m, the exchange stiffness constant $A_{ex} = 13$ pJ/m, and the magnetic damping constant $\alpha = 0.01$[20–22]. The TW displacement exhibits an inverse proportionality to the damping constant (see Supplementary Information 1). Considering its influence on the stability and range of TW dynamics, the damping constant is set to 0.01 in this study. The exchange length ($l_{ex} = \sqrt{\left(\frac{A_{ex}}{2\pi M_s^2}\right)}$) of Py can be approximately extracted from these material constants, yielding a value of 5.3 nm[23–25]. Accordingly, the cell size is set to $5 \times 5 \times 5$ nm^3. The TW displacements are calculated using two different cell sizes ($1 \times 1 \times 1$ nm^3 and $5 \times 5 \times 5$ nm^3), and the results are in good agreement with each other (see Supplementary Information 2). The head-to-head type TW, calculated using OOMMF, is centrally located in Fig. 1a. Domain walls are classified as head-to-head or tail-to-tail based on their topology. In a nanowire, the spin configuration at the center of the DW is either upward or downward. In this study, we only consider the head-to-head and up type TW. In this study, the TW displacement is indirectly extracted from the normalized magnetization component, M_x/M_s. While direct geometrical measurement from simulation snapshots is theoretically intuitive, it is highly impractical in this context. The TW possesses an inherently asymmetric spin structure, and during pulse-driven motion, both the TW and the surrounding magnetic domains undergo severe dynamic fluctuations and morphological distortions. This makes defining an exact geometric center highly ambiguous. Therefore, the macroscopic M_x/M_s ratio provides a more consistent measure of the average displacement. However, it is important to note the limitation of this method in the high-field regime: when the external field is strong enough to induce significant precessional rotation of the magnetic domains themselves (unrelated to actual DW translation), the M_x/M_s value becomes highly fluctuating.

Results and discussion

Out-of-plane magnetic field pulse driven TW dynamics

First, an OOP magnetic field pulse (B_{OOP}) = 100 mT is applied, and the TW displacement (black line) together with the normalized magnetization (M_z/M_s) of the system (red line) is plotted as a function of the simulation time (see Fig. 2a). The rise time (RT), pulse width (or duration), and fall time (FT) of the magnetic field pulse play a crucial role in determining the magnetization dynamics. In Fig. 2a, RT, pulse width, and FT are set to 10 ps, 10 ns, and 10 ps, respectively. The simulation time step is fixed at 1 ps.

Once B_{OOP} is applied to the TW, the Landau–Lifshitz–Gilbert (LLG) equation dictates that a precession torque is immediately exerted throughout the entire system, causing the TW to begin moving in the direction set by the precession torque. Simultaneously, a damping torque arises, whose magnitude is proportional to the amount of magnetization change induced by the precession torque. Consequently, the TW initially moves at a very high velocity, but its displacement gradually saturates due to the counteracting damping torque. In other words, the TW continues to move until the precession and damping torques reach a dynamic balance. During this process, M_z/M_s also converges to a constant value, reflecting the same equilibrium between the two torques. The system eventually reaches a new equilibrium state, which we define as stage 1.

At $t = 10$ ns, when OOP field pulse is removed, the TW exhibits dynamics that are essentially opposite to those described above. The system behaves as if a negative OOP field pulse is applied to a previously field-free state, and the TW rapidly and symmetrically returns toward its initial position. Again, the competition between the precession and damping torques governs the motion, and after sufficient time, both the TW displacement and M_z/M_s converge to zero. We define this relaxation process as stage 2.

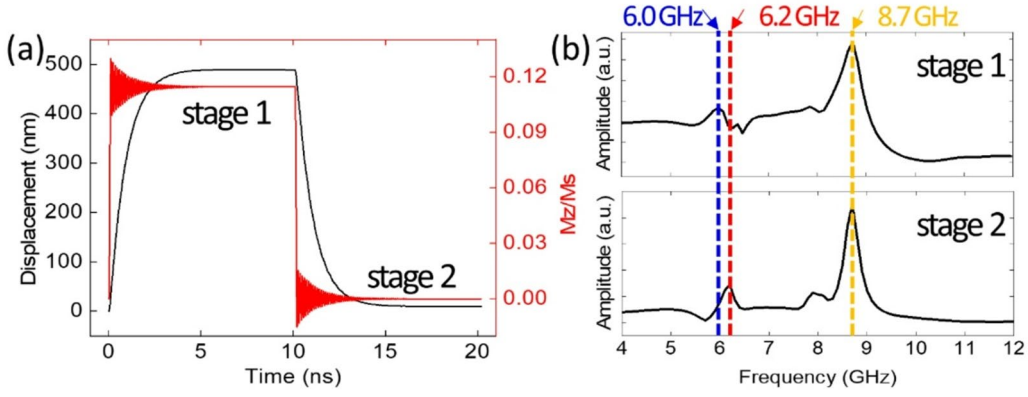

Fig. 2. Out-of-plane magnetic field pulse-driven TW dynamic and frequency analysis (**a**) Time-evolution of the TW displacement (black line) and normalized magnetization (M_z/M_s, red line) during the application (Stage 1) and removal (Stage 2) of an out-of-plane magnetic field pulse. (**b**) Fast Fourier Transform (FFT) spectra of the magnetization signals in Stage 1 and Stage 2.

On a macroscopic timescale, the TW may appear stationary; however, during the application and removal of B_{OOP}, it undergoes rapid forward and backward motion. The key factors controlling this TW dynamics are the precession and damping torques. To explain their relationship, we analyze the magnetization signals (M_z/M_s) in both stage 1 and stage 2 in the frequency domain using the Fast Fourier Transform (FFT) method. The FFT spectra in stage 1 exhibit two pronounced peaks at approximately 6.0 GHz and 8.7 GHz. Similarly, in stage 2, two peaks appear at 6.2 GHz and 8.7 GHz. The physical origins of the two observed frequencies can be interpreted as follows. First, the ferromagnetic resonance (FMR) frequency in thin films can be reasonably approximated and understood using the Kittel formula[26,27].

$$f = \frac{\gamma}{2\pi}\sqrt{[H_{\mathrm{ext}} + (N_y - N_x)\,M_s]\,[H_{\mathrm{ext}} + (N_z - N_x)\,M_s]}, \tag{1}$$

where N_x, N_y, and N_z denote the demagnetizing factors are determined by the geometry of the Py nanowire. To validate the simulation results analytically, we first summarize the material parameters and geometric dimensions of the Py nanowire utilized in this study. The magnetic flux density ($\mu_0 M_s$) of approximately 1.08 T. The gyromagnetic ratio ($\gamma/2\pi$) is assumed to be approximately 28 GHz/T, a standard value for Py. The effective magnetic field experienced by the spins within the nanowire is governed by the shape anisotropy, which varies along the principal axes (*x*, *y*, *z*). This dependence is quantified by the demagnetizing factors N_x, N_y, and N_z, which should satisfy the sum rule $N_x + N_y + N_z = 1$.

Based on the nanowire geometry, the demagnetizing factors are estimated as $N_x \approx 0$ along the longitudinal axis due to the high aspect ratio, $N_x \approx 0.9$ along the out-of-plane axis reflecting the thin-film nature, and $N_x \approx 0.1$ along the transverse axis owing to the finite width. This frequency corresponds to an intrinsic resonance mode arising from the coupling of the demagnetizing fields along the thickness (*z*) and width (*y*) directions, as described by Kittel's formula following Eq. 1. Since this mode is observed in Stage 2 in the absence of an external magnetic field, the calculation is performed assuming $H_{\mathrm{ext}} = 0$. This constant peak corresponds to the intrinsic resonance of the thin film, dominated by the strong demagnetizing field in the thickness direction, which is so-called "intrinsic FMR mode" following:

$$f = \frac{\gamma}{2\pi}\mu_0\sqrt{(N_y M_s)\,(N_z M_s)}. \tag{2}$$

By substituting all relevant parameters into Eq. (2) and calculating the higher DW frequency (f_{high}), we obtain a value of approximately $f_{\mathrm{high}} \approx 9.07$ GHz, which is in excellent agreement with the OOMMF simulation results of 8.7 GHz[28,29].

For the cases of lower FFT peak (f_{low}) positions such as 6.0 GHz and 6.2 GHz, these modes relate to the DW oscillating within the hard-axis potential well (width direction, N_y) and the formula is expressed as:

$$f_{\mathrm{low}} \propto \frac{\gamma}{2\pi}(\mu_0 N_y M_s + B_{\mathrm{eff}}). \tag{3}$$

In Stage 1, the external field (B_{OOP} = 100 mT) interacts with the spins, shifting the frequency to 6.0 GHz. In Stage 2, with the field removed (B_{OOP} = 0 mT), the system relaxes to its natural oscillation frequency of 6.2 GHz, determined purely by the internal anisotropy[30,31].

Field dependent TW motion by OOP magnetic field pulses

Figure 3 presents the calculated results of the TW displacement as a function of the out-of-plane magnetic field strength. The magnetic field pulse profile is fixed with a rise time and fall time of 10 ps and a duration of 5 ns. Figure 3a illustrates the TW displacements in the low-field regime. As the field strength increases from B_{OOP} = 100 mT to 200 mT, the TW displacement increases accordingly. However, at B_{OOP} = 200 mT, the displacement curve exhibits significant fluctuations. The physical origin of these fluctuations lies in the precession of the magnetic domains induced by the OOP magnetic field. Because the TW displacement is calculated based on the ratio between M_s and M_x, any precessional motion within the domains is reflected as an oscillation in the displacement value.

For higher B_{OOP}, the fluctuations of the magnetic domains become more pronounced, as shown in Fig. 3b. A distinct transition in the DW dynamics is observed when the B_{OOP} strength reaches 300 mT. Upon the application of the OOP magnetic field pulse, the TW and surrounding magnetic domains are strongly affected by the precessional torque. Before the damping torque can effectively suppress this precession, the magnetization within the domains begins to rotate beyond 180 degrees.

To support the observations in Fig. 3b, magnetization snapshots at B_{OOP} = 300 mT are provided in Fig. 3c with a time interval of 20 ps. At *t* = 0 ps, the TW is initially located at the center of the nanowire. When B_{OOP} = 300 mT is applied, the TW begins to move along the +*x*-direction. Concurrently, two individual magnetic domains with opposite initial magnetizations start to rotate beyond 180 degrees. Consequently, the TW collapses at approximately *t* = 60 ps. By *t* = 100 ps, the TW has completely disintegrated to the point where its structure is no longer discernible (See Supplementary Information 3 and Supplementary Movie 1).

Therefore, TW dynamics are not only dependent on the magnitude of B_{OOP} and the damping constant, but are also significantly influenced by the rise and fall times, which determine the rate of change of B_{OOP} per unit time (dB_{OOP}/dt).

The strong dependence of the TW displacement on the RT can be quantitatively understood by comparing the RT with the intrinsic DW resonance frequencies (~ 6.0 and 8.7 GHz) identified in Sect. 3.1. These frequencies correspond to natural precessional periods (T_{res}) of approximately 160 ps and 110 ps. In the fast RT regime

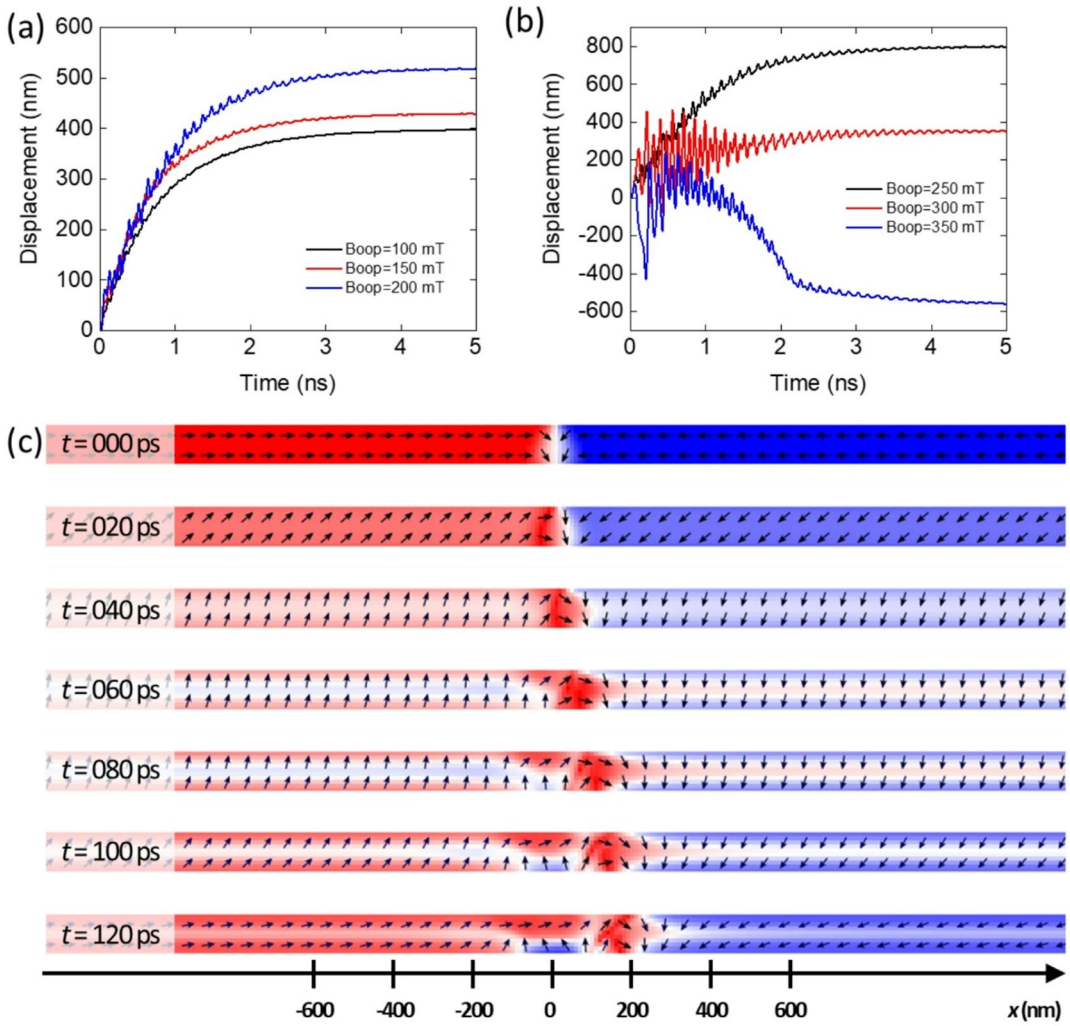

Fig. 3. Field-dependent TW motion (**a**) TW displacements as a function of time for the low-field regime (B_{OOP} = 100 mT, 150 mT and 200 mT). (**b**) TW displacements for the high-field regime (B_{OOP} = 250 mT, 300 mT and 350 mT). (**c**) Time-resolved magnetization snapshots at B_{OOP} = 300 mT with a time interval of 20 ps. The arrows and color scale represent the magnetization directions. All simulations were performed with a pulse rise time and fall time of 10 ps.

(e.g., 100 ps to 200 ps), the RT is comparable to T_{res}, satisfying a resonance condition where the transient field effectively couples with the intrinsic precessional modes, yielding efficient DW displacement. Conversely, an ultrafast RT (1 ps, $\mathrm{RT} \ll T_{\mathrm{res}}$) acts as a severe impulse that primarily excites chaotic internal spin-waves, limiting the net displacement. In the slow RT regime ($\mathrm{RT} \gg T_{\mathrm{res}}$), the field changes adiabatically, avoiding resonance and maintaining a continuous balance between precessional and damping torques.

Rising time dependent TW motions

As previously discussed, the rise time (RT) and fall time (FT) are critical factors governing the dynamics of TWs driven by B_{OOP} fields. In this section, we systematically investigate the dependence of TW displacement on RT. The simulations are performed by dividing the RT into two distinct regimes: a relatively fast RT regime ranging from 1 ps to 0.5 ns (see Fig. 4a) and a slower RT regime ranging from 1 ns to 5 ns (see Fig. 4b). In these figures, the B_{OOP} field pulse profiles corresponding to individual RTs are indicated by dashed lines, while the resulting TW displacements are represented by solid lines. The magnitude of the B_{OOP} field is fixed at 100 mT for all simulations concerning RT-dependent TW displacement.

In the fast RT regime (RT = 1 ps ~ 500 ps), a rapid increase in TW displacement is observed immediately upon the application of the magnetic field pulse. Notably, significant fluctuations are observed in the TW displacement curve for the case of RT = 1 ps. This behavior can be interpreted using the Landau–Lifshitz–Gilbert (LLG) equation. Although the OOMMF framework fundamentally solves the Landau–Lifshitz (LL) equation, we employ the LLG equation for our analysis because the two formalisms are mathematically equivalent when the damping constant is sufficiently small[32].

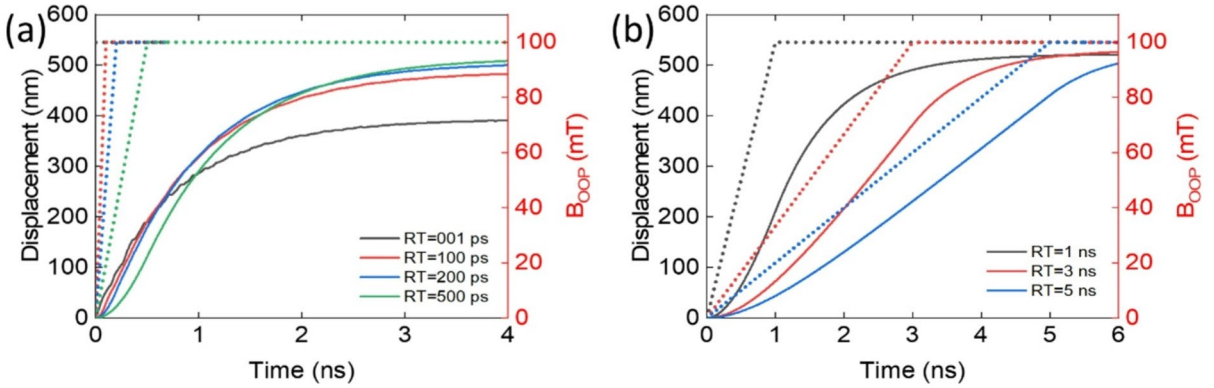

Fig. 4. Rise time dependence of TW displacements (**a**) TW displacement (solid lines) in response to B_{OOP} field pulses (dashed lines) in the fast RT regime (1 ps to 500 ps). (**b**) TW displacement in the slower RT regime (1 ns to 5 ns). The magnitude of the B_{OOP} field is fixed at 100 mT for all profiles.

$$\frac{d\boldsymbol{m}}{dt} = -\gamma\, \boldsymbol{m} \times H_{\text{eff}} + \alpha\, \boldsymbol{m} \times \frac{d\boldsymbol{m}}{dt}. \tag{4}$$

According to Eq. (4), an RT of 1 ps corresponds to a frequency of 1 THz. Consequently, the B_{OOP} field reaches its peak of 100 mT before the magnetization completes a single rotation induced by the precession torque. Under these conditions, the time derivative of the magnetization is maximized. Specifically, the maximization of the damping torque term ($\boldsymbol{m} \times \frac{d\boldsymbol{m}}{dt}$) causes the system to undergo severe internal fluctuations, suggesting a high probability of spin-wave excitations oscillating within the wall structure. As a result, the TW displacement fails to increase continuously, saturating at approximately 390 nm. In contrast, other profiles within the RT < 0.5 ns range exhibit saturation of TW displacement at levels approaching 500 nm.

For the slower RT regime RT = 1 ns ~ 5 ns, the gradual increase of the B_{OOP} field allows for a balanced interplay between the precession and damping torques during TW motion. Consequently, it is observed that the TW reaches its maximum displacement with a noticeable time delay relative to the field application.

In-plane field assisted depinning field calculations

The non-equilibrium dynamics of a TW driven by an out-of-plane magnetic field pulse typically result in zero net displacement, as the TW tends to return to its initial equilibrium position after the pulse is removed. To utilize this behavior in spintronic applications, such as racetrack memory, a mechanism to trap the TW at a specific location is required; this technique is referred to as "dynamic pinning" and has been extensively discussed in previous studies[33–35].

In this study, we focus on the depinning mechanism of TWs. Specifically, we investigate the critical B_{OOP} field required for depinning in the presence of a weak static in-plane magnetic field (B_x). As illustrated in the inset of Fig. 5, the initial spin configuration consists of a TW pinned at a geometrical notch with dimensions of 5 × 5 nm^2. To establish the equilibrium state under the applied in-plane field, a relaxation process of 10 ns is performed prior to the pulse application. Subsequently, we calculate the threshold B_{OOP} field intensity required to induce depinning. An in-plane bias field is introduced because DW based racetrack memory typically requires unidirectional data propagation. Consequently, applying B_x facilitates TW depinning, thereby minimizing the energy consumption required for information transport.

As depicted in Fig. 5, the critical B_{OOP} field required for depinning is 65 mT in the absence of an in-plane field ($B_x = 0$). However, this threshold decreases monotonically as B_x increases. Simulations are performed for B_x values up to 4.8 mT, at which point the critical B_{OOP} field drops to 5 mT. For in-plane fields exceeding 4.8 mT, the TW depins spontaneously without the assistance of a B_{OOP} field. Remarkably, the critical B_{OOP} field required for TW depinning exhibits a nearly linear dependence on the magnitude of B_x[31].

The physical mechanism behind this 'dynamic pinning' can be comprehensively understood through the effective potential energy landscape of the nanowire. A geometrical notch acts as a localized attractive potential well (energy minimum) for the TW. During the application of the B_{OOP} pulse, the precessional torque imparts sufficient kinetic energy for the TW to overcome the local potential barriers, facilitating motion. However, during the pulse fall time, the precessional driving torque rapidly diminishes, and the TW's kinetic energy is actively dissipated via the damping torque. If the TW arrives at the spatial vicinity of a notch precisely during this deceleration phase, it lacks the requisite energy to overcome the local potential barrier and inevitably falls into the energy minimum. This synchronization of the pulse fall time with the attractive potential of the notch explains the dynamic trapping mechanism, which aligns well with the kinetic pinning and dynamic potential models discussed in previous literature[33–35], as well as recent advancements in dynamic magnetization control[22,25,36].

Multi-step DW motions accompanied with dynamic pinning at successive notches

To realize magnetic field pulse-driven racetrack memory utilizing OOP-induced TW dynamics, demonstrating reliable sequential operation is crucial. This involves not only the dynamic depinning process but also the ability

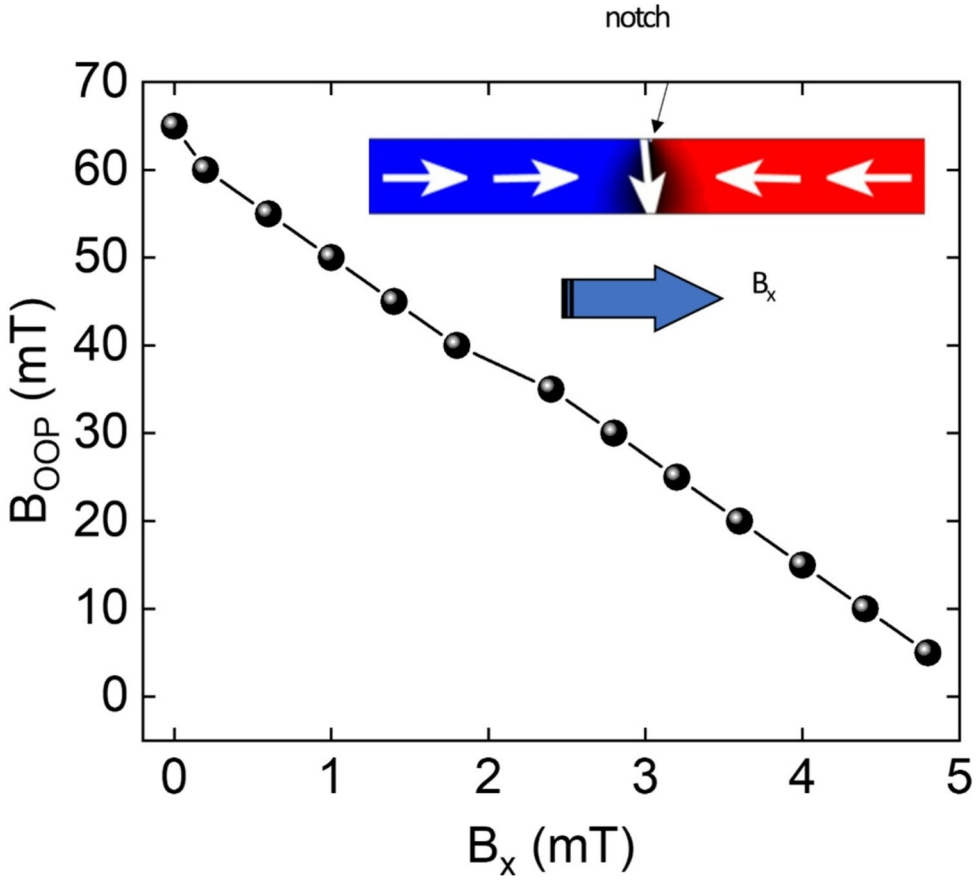

Fig. 5. Dependence of the critical out-of-plane depinning field with the in-plane bias field (B_x). The threshold B_{OOP} required to depin a TW from a notch decreases linearly with increasing B_x. The inset shows the initial spin configuration of a TW pinned at a 5 × 5 nm^2 geometrical notch.

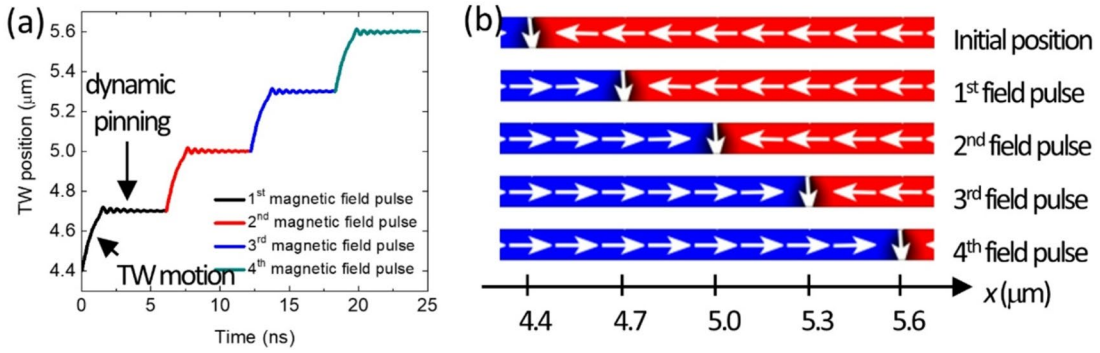

Fig. 6. Multi-step TW motion with dynamic pinning at successive notches. (**a**) Time-evolution of the TW position during four consecutive cycles of depinning and propagation, followed by dynamic pinning at the next notch. (**b**) Magnetic configuration snapshots at the initial state (t =0 ns) and TW positions (configurations) after the application of sequential B_{OOP} field pulses.

of the TW to move unidirectionally over multiple cycles and successfully re-pinned at notches with the identical intervals. Figure 6 presents simulation results demonstrating four consecutive cycles of TW motion, consisting of dynamic depinning by a B_{OOP} field pulse, propagation, and subsequent dynamic pinning at the adjacent notch. Figure 6a illustrates the calculated time-evolution of the TW position under these four successive pulses.

To ensure a stable depinning process, the B_{OOP} pulse profile is fixed with the following parameters: a rise time (RT) of 0.1 ns, a duration of 3 ns, a fall time (FT) of 3 ns, and a peak amplitude of 100 mT. The notches are arranged with a periodicity of 300 nm. Unlike in previous simulations, the FT is deliberately set to a relatively slow 3 ns to prevent the TW from escaping the notch (overshooting) during the dynamic pinning phase, which

can occur with faster field decay. Consequently, the total duration for one complete cycle—encompassing depinning from one notch to dynamic pinning at the next—is 6.1 ns (0.1 ns + 3 ns + 3 ns).

Initially, the TW is positioned at the 4.4 μm mark of a 10 μm-long Py nanowire (see Fig. 6b). Upon application of the OOP field, the TW is immediately depinned by the precession torque and begins to propagate toward the right. At t = 3.1 ns, the TW approaches the adjacent notch located 300 nm away, where it becomes dynamically pinned and undergoes spatial oscillations around the notch center. These oscillations are clearly visible in the TW position trajectory shown in Fig. 6a. The gradual decay of the B_{OOP} field over the 3 ns FT facilitates the stabilization of the TW, ensuring secure pinning at the notch. This sequence is repeated four times. The simulation confirms that the TW is successfully depinned and subsequently dynamically pinned at each successive notch position without failure for all applied pulses.

Figure 6b displays magnetic configuration snapshots at the initial state (t = 0 ns) and at the conclusion of each pulse cycle (t = 6.1, 12.2, 18.3, and 24.4 ns). It is evident that the TW retains an identical topological structure across all five distinct positions. These results strongly support the feasibility of realizing a racetrack memory device based on magnetic field pulse-driven TW motion.

Impulsive TW propagation via localized magnetic field pulses

As discussed previously, the B_{OOP} field pulse-driven TW motion exhibits a significantly higher initial velocity compared to conventional current-induced TW motion via spin-transfer torque. Furthermore, because this method does not require direct current injection into the magnetic nanowire, it offers the distinct advantage of being largely free from the effects of Joule heating. However, it is crucial to demonstrate net TW displacement within a defect-free magnetic nanowire to practically implement this mechanism in racetrack memory architectures.

In the earlier sections, because the B_{OOP} field is applied globally across the entire system, dynamic pinning effect to fix the TW at a specific position after a single pulse cycle is mandatory. This approach requires continuous artificial notches and asymmetric magnetic field pulse profiles varying RT and FT. To overcome this structural limitation and realize TW displacement in a defect-free nanowire, we now introduce a localized B_{OOP} field driven impulsive TW propagation.

Figure 7a presents the schematic configuration of the TW motion driven by a localized B_{OOP} field. The TW is initially positioned at the center of the nanowire, and the localized B_{OOP} field is applied exclusively within a restricted spatial window ranging from x = −100 nm to x = + 100 nm. The total simulation time is set to 6 ns, with the B_{OOP} duration fixed at 4 ns. For the localized B_{OOP}, values of 100 mT and 150 mT are selected. When the pulse is applied, the precessional torque instantly accelerates the TW and pushes it out of the magnetic field region. The TW continues to propagate ballistically beyond the localized field area until the transient dynamics are eventually saturated by intrinsic magnetic damping (see Fig. 7b).

Figure 7c shows sequential snapshots of the TW propagation between t = 0.0 ns and t = 1.4 ns. TW is initially positioned at the center and the TW is driven by the localized B_{OOP} field applied within the yellow shaded region. The snapshots clearly illustrate the TW escaping this localized field area and moving ballistically to the right, which inherently prevents reverse motion when the magnetic pulse is later removed. Consequently, even when symmetric rise and fall times (RT = FT = 10 ps) are utilized in this simulation, the TW does not undergo the reverse dynamics to return to its initial position, simply because it resides outside the localized B_{OOP} area when the pulse is removed.

Conclusions

The OOP magnetic field pulse-driven motion of a TW was investigated through micromagnetic simulations. The magnetization dynamics are found to be governed by the competition between the precession and damping torques, which cause the TW to displace and subsequently return to its initial state upon field removal. The TW dynamics are further characterized in the frequency domain, where two distinct modes are identified: an intrinsic ferromagnetic resonance (FMR) mode at approximately 8.7 GHz and an oscillation mode related to the hard-axis potential well at 6.0–6.2 GHz. The TW structural integrity is shown to be preserved only in the low-field regime, while in the high-field regime B_{OOP} = 250 mT, the TW structure is observed to collapse. Moreover, the importance of the magnetic field rise time (RT) is demonstrated, with an ultrafast RT = 1 ps causing severe internal fluctuations. To enable continuous motion, a geometrical notch is introduced, and the critical B_{OOP} field for depinning is found to be linearly reduced with the application of an in-plane bias field B_x. Finally, the feasibility of a racetrack memory device is strongly supported by demonstrating four consecutive cycles of depinning and dynamic pinning at successive notches.

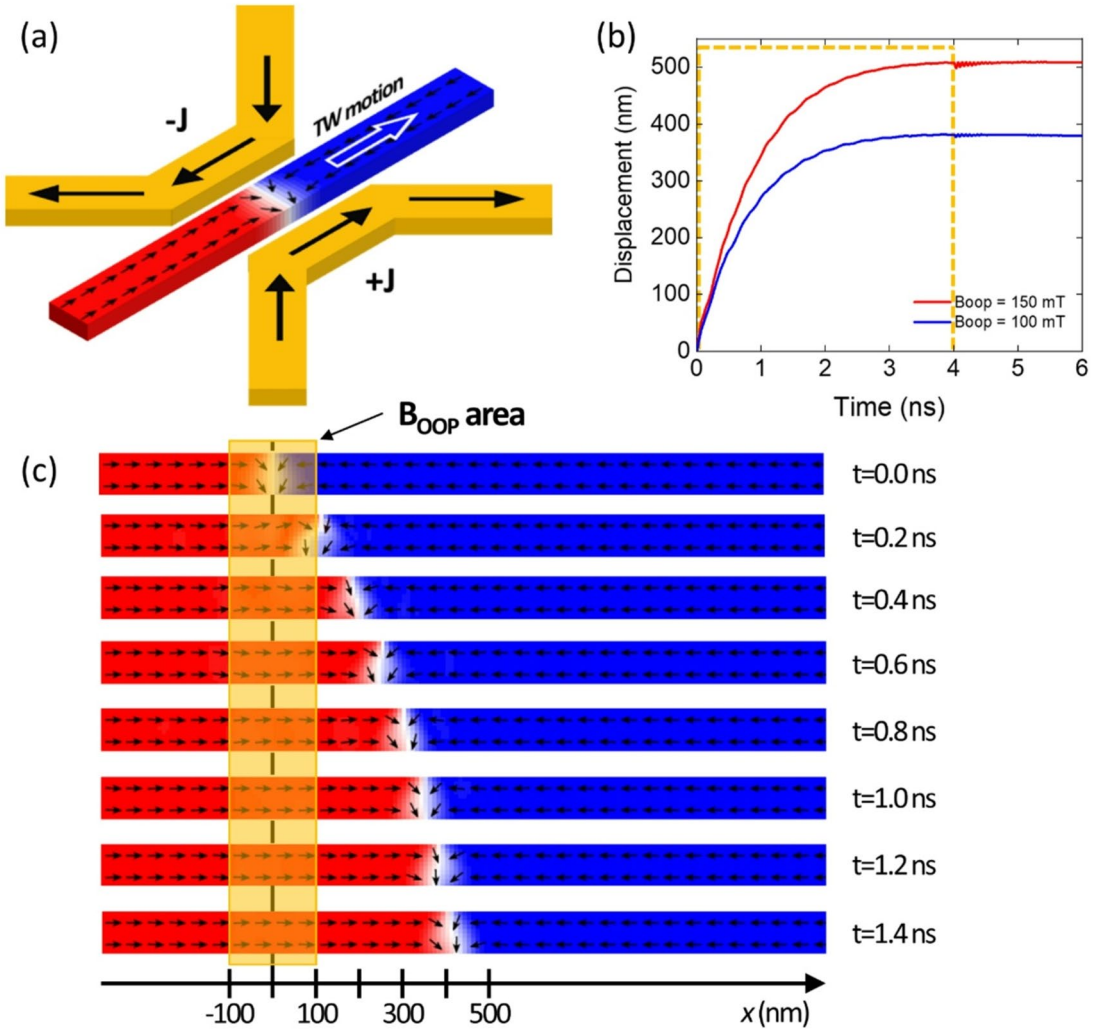

Fig. 7. Impulsive TW propagation driven by a localized magnetic field pulse. (**a**) Schematic illustration of the TW motion in a defect-free magnetic nanowire. (**b**) Time-dependent displacements of the TW for localized B_{OOP} magnitudes of 100 mT (blue line) and 150 mT (red line). The yellow dashed lines indicate the magnetic field pulse profile with the 4 ns duration during the 6 ns total simulation time. (**c**) Sequential snapshots of the magnetization dynamics from $t = 0.0$ ns to $t = 1.4$ ns. The TW is rapidly accelerated by the precessional torque and ballistically escapes the localized B_{OOP} area ($x = -100$ nm to $+100$ nm, yellow box).

Data availability

The datasets generated during and/or analyzed during the current study are available from the corresponding author on reasonable request.

Received: 20 January 2026; Accepted: 20 April 2026
Published online: 27 April 2026

References

1. Parkin, S. S. P., Hayashi, M. & Tomas, L. Magnetic domain-wall racetrack memory. *Science* **320**, 190–194 (2008).
2. Beach, G. S. D., Tsoi, M. & Erskine, J. L. Current-induced domain wall motion. *J. Magn. Magn. Mater.* **320**, 1272–1281 (2008).
3. Kim, K. J. et al. Current-induced magnetic domain wall motion below intrinsic threshold triggered by Walker breakdown. *Nat. Commun.* **3**, 671 (2012).
4. Guan, Y. et al. Highly efficient current-induced domain wall motion in a room-temperature vdW ferromagnet via spin-orbit torque. *Nat. Commun.* **16**, 10255 (2025).
5. Allwood, D. A. et al. Magnetic domain-wall logic. *Science* **309**, 1688–1692 (2005).
6. Luo, Z. et al. Current-driven magnetic domain-wall logic. *Nature* **579**, 214–218 (2020).
7. Currivan-Incorvia, J. A. et al. Logic circuit prototypes for three-terminal magnetic tunnel junctions with mobile domain walls. *Nat. Commun.* **7**, 10275 (2016).
8. Kumar, D. et al. Ultralow energy domain wall device for spin-based neuromorphic computing. *ACS Nano*. **17**, 6261–6274 (2023).
9. Zhang, X., Ezawa, M. & Zhou, Y. Magnetic skyrmion logic gates: Conversion, duplication and merging of skyrmions. *Sci. Rep.* **5**, 9400 (2015).

10. Shen, L., Zhou, Y. & Shen, K. Programmable skyrmion-based logic gates in a single nanotrack. *Phys. Rev. B* **107**, 054437 (2023).
11. Kim, D.-H. et al. A method for compensating the Joule-heating effects in current-induced domain wall motion. *IEEE Trans. Magn.* **49**, 3207–3210 (2013).
12. Curiale, J. et al. Joule heating and current-induced domain wall motion. *J. Appl. Phys.* **112**, 103922 (2012).
13. Fan, L., Hu, J., Su, Y. & Zhu, J. Influence of temperature on current-induced domain wall motion and its Walker breakdown. *J. Magn. Magn. Mater.* **401**, 484–487 (2016).
14. Kim, J.-S. et al. Synchronous precessional motion of multiple domain walls in a ferromagnetic nanowire by perpendicular field pulses. *Nat. Commun.* **5**, 3429 (2014).
15. Peeters, M. J. G. et al. Precession-torque-driven domain-wall motion in out-of-plane materials. *AIP Adv.* **7**, 055921 (2017).
16. Kim, J. S., Lee, H. J., Hong, J. I. & You, C. Y. Field driven magnetic racetrack memory accompanied with the interfacial Dzyaloshinskii-Moriya interaction. *J. Magn. Magn. Mater.* **455**, 45–53 (2018).
17. Cho, J., Kim, K.-W., Lee, M.-J., Lee, H.-J. & Kim, J.-S. Non-equilibrium chiral domain wall dynamics excited by transverse magnetic field pulses.. *J. Phys. Condens. Matter* **33**, 015803 (2021).
18. COMSOL Multiphysics® v. 6.2. www.comsol.com. Stockholm, Sweden. (2023).
19. Donahue, M. J. & Porter, D. G. OOMMF User's Guide, Version 1.0. (1999). https://math.nist.gov/oommf/
20. Bhattacharjee, P. & Barman, S. Observation of higher-order gyrotropic modes and energy transfer in cylindrical ferromagnetic nanodots-based square lattices.. *J. Phys. Chem. Solids* **198**, 112475 (2025).
21. Bhattacharjee, P. & Barman, S. Excitation modes for spin waves in a two-dimensional magnetic vortex lattice.. *Phys. Status Solidi A* **262**, 2500070 (2025).
22. Al Bahri, M., A.-Kamiyani, S. & Saavedra, E. Engineering of magnetic domain walls via antidot geometry for advanced multi-state memory applications.. *Sci. Rep.* **16**, 4585 (2026).
23. Thiaville, A., Nakatani, Y., Miltat, J. & Suzuki, Y. Micromagnetic understanding of current-driven domain wall motion in patterned nanowires.. *Europhys. Lett.* **69**, 990–996 (2005).
24. Wang, J. et al. Magnetic domain wall engineering in a nanoscale permalloy junction.. *Appl. Phys. Lett.* **111**, 072401 (2017).
25. Al Bahri, M. & Shiaa, R. Chirality-dependent dynamics and pinning of transverse domain wall in constricted nanowires.. *Phys. Status Solidi A* **221**, 2300906 (2024).
26. Lee, K. et al. The buffer layer effect of the exchange stiffness constants on Co thin film.. *J. Magn. Magn. Mater.* **512**, 167057 (2020).
27. Jung, J. et al. Modulations of interfacial magnetic properties using structurally inverted magnetic tri-layer systems: Toward skyrmion formation. *Appl. Phys. Lett.* **118**, 262408 (2021).
28. Yoon, J., You, C. Y., Jo, Y., Park, S. Y. & Jung, M. H. Micromagnetic analysis of magnetic noise in ferromagnetic nanowires. *J. Korean Phys. Soc.* **57**, 1594–1599 (2010).
29. Yoon, J., You, C.-Y., Jo, Y., Park, S.-Y. & Jung, M.-H. Magnetic domain wall ferromagnetic resonance in ferromagnetic nanowires due to the spin transfer torque. *Appl. Phys. Express* **4**, 063006 (2011).
30. Lee, K.-S., Han, D.-S. & Kim, S.-K. Dynamics of magnetic domain walls in magnetic nanowires: Ferromagnetic resonance. *Phys. Rev. Lett.* **102**, 127202 (2009).
31. Kim, J.-S. et al. Interaction between propagating spin waves and domain walls on a ferromagnetic nanowire. *Phys. Rev. B* **85**, 174428 (2012).
32. Kim, J.-S., Hwang, H.-K. & You, C.-Y. Non-equilibrium dynamic reversal of in-plane ferromagnetic elliptical disk. *J. Magn. Magn. Mater.* **445**, 103–109 (2018).
33. Ahn, S.-M., Kim, D.-H. & Choe, S.-B. Kinetic and static domain-wall pinning at notches on ferromagnetic nanowires. *IEEE Trans. Magn.* **45**, 2478–2480 (2009).
34. Kunz, A. & Priem, J. D. Dynamic notch pinning fields for domain walls in ferromagnetic nanowires. *IEEE Trans. Magn.* **46**, 1559–1561 (2010).
35. Pi, U.-H. et al. Static and dynamic depinning processes of a magnetic domain wall from a pinning potential. *Phys. Rev. B* **84**, 024426 (2011).
36. Al Bahri, M., Al-Kamiyani, S., Al Hinaai, M. M. & Ali, N. Thermal influence on chirality-driven dynamics and pinning of transverse domain walls in Z-Junction magnetic nanowires. *Symmetry* **17**, 1184 (2025).

Acknowledgements

This work is supported by the National Research Foundation of Korea (NRF) and funded by the Ministry of Science and ICT (2021M3F3A2A01037526) and the DGIST R&D Programs (26-ET-02).

Author contributions

J.-S.K. conceived the main idea. J.-S.K. performed numerical simulations, J.C. and W.S.Y. carried out all micromagnetic simulations, analyzed the results. J.-S.K. prepared some figures, and J.C. and W.S.Y. wrote the manuscript, and all authors discussed the results.

Declarations

Competing interests

The authors declare no competing interests.

Additional information

Supplementary Information The online version contains supplementary material available at https://doi.org/10.1038/s41598-026-50309-4.

Correspondence and requests for materials should be addressed to J.-S.K.

Reprints and permissions information is available at www.nature.com/reprints.

Publisher's note Springer Nature remains neutral with regard to jurisdictional claims in published maps and institutional affiliations.

Open Access This article is licensed under a Creative Commons Attribution-NonCommercial-NoDerivatives 4.0 International License, which permits any non-commercial use, sharing, distribution and reproduction in any medium or format, as long as you give appropriate credit to the original author(s) and the source, provide a link to the Creative Commons licence, and indicate if you modified the licensed material. You do not have permission under this licence to share adapted material derived from this article or parts of it. The images or other third party material in this article are included in the article's Creative Commons licence, unless indicated otherwise in a credit line to the material. If material is not included in the article's Creative Commons licence and your intended use is not permitted by statutory regulation or exceeds the permitted use, you will need to obtain permission directly from the copyright holder. To view a copy of this licence, visit http://creativecommons.org/licenses/by-nc-nd/4.0/.

© The Author(s) 2026